Article type: Research Paper

Title The influence of carbon source and catalyst nanoparticles on CVD synthesis of CNT aerogel

Author(s), and Corresponding Author(s): Christian Hoecker[a], Fiona Smail[a], Martin Pick[b], Adam Boies[a,*]

[a] University of Cambridge, Department of Engineering, Cambridge CB2 1PZ, United Kingdom

[b] Q-Flo Limited, BioCity, Pennyfoot Street, Nottingham NG1 1GF, United Kingdom

Abstract

The floating catalyst chemical vapour deposition (FC-CVD) method is unique in providing the capability for continuous carbon nanotube (CNT) synthesis at an industrial scale from a one-step continuous gas-phase process. Controlling the formation of the iron-based catalyst nanoparticles is widely recognized as a primary parameter in optimizing both CNT product properties and production rate. Herein the combined influences of pyrolytic carbon species and catalytic nanoparticles are both shown to influence CNT aerogel formation. This work studies the source of carbon in the formed CNTs, the location of aerogel formation, the in-situ behaviour of catalyst nanoparticles and the correlated morphology of the resultant CNTs. Axial measurements using isotopically-labelled methane (CH_4) demonstrate that carbon within all CNTs is primarily derived from CH_4 rather than some of the early-forming CNTs being predominantly supplied with carbon via thermal decomposition of catalytic precursor components. Quantification of CNT production along the axis of the reactor definitively

* Corresponding author. Tel: 01223 332600. E-mail: a.boies@eng.cam.ac.uk

dispels the notion that injection parameters influence CNT formation and instead shows that bulk CNT formation occurs near the reactor exit regardless of the carbon source (CH_4, toluene or ethanol). Supply of carbon to different reactor locations indicates that CNT aerogel formation will occur even when carbon is delivered near the exit of the reactor so long as the carbon source reaches a sufficient temperature (>1000 °C) to induce pyrolysis. These results give an indication of how future large-scale CNT reactors may be optimized and controlled by modifying downstream catalyst and carbon delivery.

Keywords

Chemical vapor deposition; CNT synthesis; CNT aerogel; Catalytic synthesis; Pyrolysis

1. Introduction

At the nanoscale, individual CNTs have been shown to possess significantly improved mechanical, thermal and electrical properties compared to existing materials. However, their applications have been limited due to the inability to produce CNTs as continuous macroscopic matrices on an industrial scale. Interest in producing macroscopic assemblies of CNTs, driven by their unique combination of properties continues to stimulate academic research around the world and to drive forward industrial development. At least two companies are currently working with research groups to commercialize FC-CVD technology[1,2], others are exploring the liquid-crystal spinning route[3] and dry-spinning techniques continue to develop[4–6]. The FC-CVD route, which facilitates the continuous collection of a CNT aerogel using techniques pioneered by Windle *et al*.[7] is an attractive option for scale-up due to its relative simplicity and one-step production method. A video of the process including the collection and a close-up view of the aerogel formation can be found in the supplementary material. The excitement the method continues to generate is reflected

in the academic publication trends illustrated by the bar chart in Figure 1. Over the last ten years the number of academic groups with continuous aerogel-spinning capabilities has increased to at least nine, with three new groups contributing their first publications this year[8–11]. The level of interest is of little surprise when the range of potential applications associated with these materials is considered[12,13], whether as uncondensed sheet formats, condensed filaments or post-treated matrices and is reflected in the more recent publication of applications-based reviews in areas such as electrical[14] and electro-thermal[15] properties of the materials.

Given the amount of interest in the FC-CVD process (30 published studies on the synthesis), it is surprising that the fundamental influences of precursor decomposition, and catalyst formation on CNT growth are still not well understood. However, the complexity of a multi-parameter reaction space coupled with the challenges of real-time in-situ measurements has made absolute conclusions difficult. For example, while the role of sulphur (S) in promoting CNT growth rates through the formation of iron-sulphur (Fe-S) eutectic phases on the surfaces of the catalytic particles[16] is a well-established concept, drawing on knowledge from literature on its role in the synthesis of vapour grown carbon fibers[17], proposing definitive C:Fe:S ratios for the floating catalyst CVD process is problematic when the efficiency of the reaction is poor (in the range of 1-4% based on carbon conversion to CNTs[18]) and typically losses of Fe to the reactor walls and sulphur as H_2S in the exhaust gases during the reaction remain unquantified. Conclusions regarding mechanisms controlling the influence of sulphur on CNT structure by changing either the concentration of the S-containing reagent[19–22] or the type of reagent[23], or the effect of different carbon sources on product impurity[18] may also need to be cautiously applied, especially as the majority of these are based on ex-situ characterization of the final product. Until now, schematics and hypotheses assumed

that the morphology profile of the aerogel product is determined by the catalytic growth of CNTs and related graphitic materials immediately after the initial nucleation and growth of catalytic nanoparticles. Researchers have linked the ratios of C:Fe:S and the choice of carbon sources based on their thermal decomposition temperature and whether they are oxygen-containing or not (e.g. alcohol[18], aromatic carbon[24], saturated hydrocarbon etc.) as strong determining factors in controlling product purity.

This has led to various assumptions such as i) the CNT aerogel formation process is dominated by reactions soon after the injection of reactants in the upstream portion of the reactor, ii) the impurity profile of the material (e.g. presence of large diameter, badly deformed CNT tubules, graphitically encapsulated catalytic nanoparticles and amorphous carbon deposits) is most strongly influenced by the initial catalyst precursor decomposition processes and their interaction with the carbon sources, iii) the importance of matching the thermal decomposition temperature of the carbon source with that of the catalytic nanoparticle generation to ensure good carbon availability[25]. Typical schematics as seen elsewhere[26,27] illustrate these assumptions.

However in our previous work[28], the behaviour of catalyst nanoparticles and full characterization of the nucleation, evaporation and re-nucleation of the catalytic nanoparticles along the length of a FC-CVD reactor is shown for the first time. It was found that the morphology of the CNT aerogel constituents changes significantly along the reactor axis and correlates directly with the catalytic nanoparticle behaviour. Key observations were that both the vast majority of the aerogel material and the major product impurities were formed in the latter portion of the reactor, indicating that the product formation is dominated by re-nucleation processes occurring on the downwards temperature profile of the reactor rather than by the initial decomposition of the catalytic precursors. These observations also point towards pyrolytic carbon

species being important in the aerogel formation. As a consequence of these initial observations, in this paper we present a rigorous investigation regarding the interaction of carbon species with the catalytic nanoparticles along the reactor axis. Carbon is provided to the reaction system not only from the principal carbon source but additionally in small quantities via ferrocene and thiophene catalytic precursors. In the case of CH_4 as the principal carbon source, the difference in thermal decomposition temperatures of the various components ($T_{\text{ferrocene}}<T_{\text{thiophene}}<<T_{CH_4}$) means that the thermal release of carbon and generation of pyrolytic compounds from each species occurs at a different axial reactor location. The first section of this paper determines whether the carbon released from ferrocene and thiophene disproportionately contributes to the small amount of CNT growth in the early axial locations, through the use of $C^{13}H_4$ and Raman analysis to quantify the amount of carbon from CH_4 present in the product throughout the reactor space. The study therefore investigates which carbon sources play the most dominant role in the CNT synthesis at different stages in the reactor and relates this to both the product morphology and crystallinity.

The synthesis and growth of CNTs results from a process in which catalytic assisted pyrolysis of the carbon source and decomposition of pyrolytic compounds play a major role[29,30]. In the latter sections of the paper we investigate the influence of the carbon source in the region near the reactor exit where the bulk formation of CNT aerogel occurs, and question whether ideas previously postulated about the cracking temperature of the hydrocarbon source are of importance for product control. Furthermore, the influence of pyrolytic carbon species on the aerogel formation process, due to the thermal cracking of all the carbon sources, is investigated by contrasting the rates of aerogel formation in the catalyst particle re-nucleation zone when only CH_4 is supplied (via a reverse injection configuration) compared to when pyrolysis compounds are present due to thermal decomposition in the hottest zone of the reactor. Given the relatively low carbon conversion to CNTs of typically 1-

4% in current CNT aerogel formation processes, it is important to understand where and how the reactor carbon is being used, so that methods can be developed to achieve higher conversion rates, maximizing CNT aerogel growth and controlling product quality.

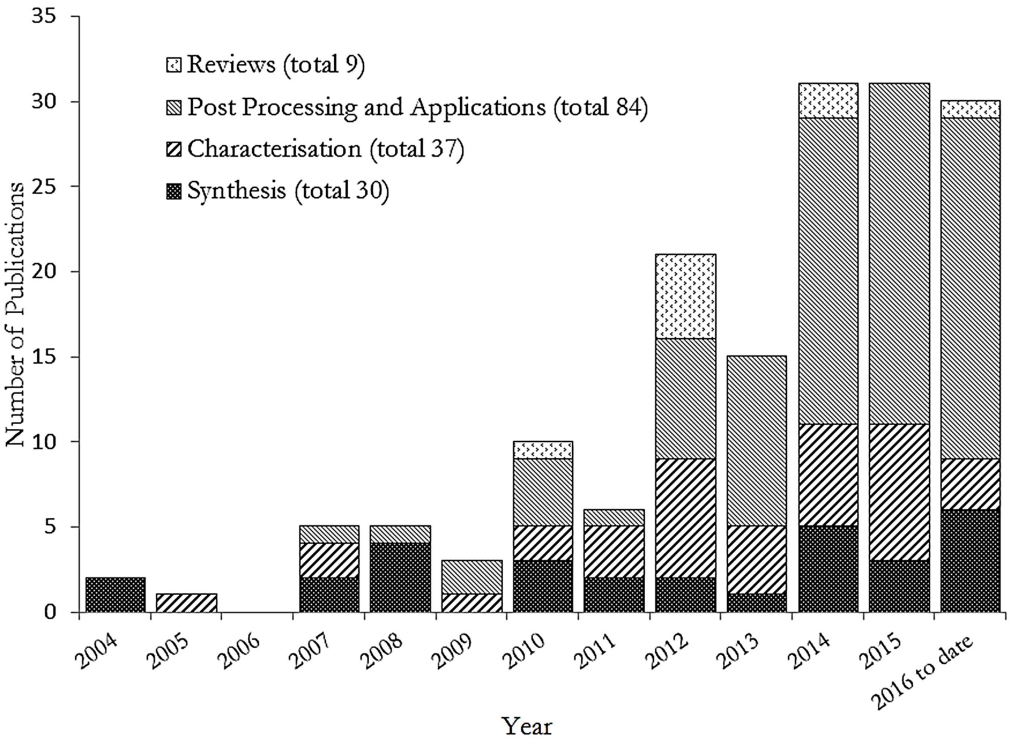

Figure 1. Bar chart showing academic publications on the FC-CVD route for continuous CNT aerogel synthesis over time (see Supplementary Table 1 for details and categorization of publications).

2. Experimental Methods

A lab-scale horizontal aerogel reactor was used for all of the experiments, which consisted of a tube furnace with an injection port at the inlet and gas exchange valve and aerogel spinner at the outlet as previously described[28]**.** The specific process parameters for each investigation are given below.

2.1. C^{13} analysis

A CNT aerogel was synthesized using $C^{13}H_4$ (Linde, >98.8), ferrocene (98% purity, Acros) and thiophene (≥ 99%, Sigma Aldrich) in H_2 (0.5 slpm, purity grade hydrogen N5.0, BOC) flowing through a quartz reactor tube (46 mm ID, 700 mm length) in a furnace set at 1200 °C. Ferrocene was supplied via a H_2 flow (40 sccm, ~1×10^{-6} mol ferrocene/min) through a sublimation pack set at 77 °C and thiophene was supplied as a vapor in a H_2 flow (10 sccm, ~1.4×10^{-5} mol thiophene/min) via a liquid bubbler held at ~0 °C. All gas flow rates were controlled by mass flow controllers (Alicat). After 8 minutes supply of ferrocene, thiophene and H_2, $C^{13}H_4$ (40 sccm) was added and was halted after a further 8 minutes, when the formation of CNT aerogel material was observed in the rear section of the reactor tube. The tube was flushed with argon (Ar) (10 sccm, purity N4.8, BOC) during cooling. The aerogel filament, stretching the length of the reactor tube, was extracted intact, split into ~50 mm long sections, and pieces from each section were mounted on microscope slides. Raman spectra were collected using a 534 nm laser (2 mW) on a Bruker Senterra I instrument fitted with plane polarization, a confocal microscope (20x objective) and a 0.5 cm^{-1} resolution grating. To calculate the C^{12}:C^{13} ratio, at least four spectra (three accumulations per spectra) were collected from different locations for each section and the results of these were averaged.

2.2. Axial Aerogel Quantification

Conditions were established for successfully spinning CNT aerogels from CH_4 (99.5%, BOC), ethanol (Sigma Aldrich, HPLC grade) and toluene (Sigma Aldrich, 99.3% purity) in an alumina tubular reactor (40 mm ID, 700 mm length, 1300 °C). For each carbon

source, ferrocene was supplied via a H_2 flow (100 sccm, ~$8x10^{-6}$ mol/min) through a sublimation pack set at 94 °C and thiophene vapour was supplied via H_2 passing through a liquid bubbler (100 sccm, $1.1x10^{-4}$ mol/min) set at ~0 °C. These supply rates were higher than those used for the $C^{13}H_4$, so that a greater quantity of aerogel was produced, but using similar ratios of the two precursors, assuming complete saturation of the gas passing through the saturator, so that there would be minimal impact on the synthesis conditions. CH_4 was supplied at 120 sccm while ethanol and toluene were both injected via a syringe pump at 8 ml/h and 2.5 ml/h respectively. All were carried through the reactor in a H_2 flow of 1.4 slpm (purity grade hydrogen N5.0, BOC).

For each hydrocarbon source a series of experiments were carried out, with new and separate pre-weighed circular alumina particle filters used for each data point (40 mm diameter, pore size 1 mm^2, filter depth minimum ~30 mm, filter efficiency >99% for particles <10 nm diameter and >90% for particles 10 nm < d < 20 nm, see Fig. S2). These were placed at different axial positions in the reactor each time. The reagents were supplied, in quantities known to give aerogel-formation, for a set length of time, with any aerogel material downstream of the particle filter being removed as it formed. Depending on the position of the filter and potential clogging of the tube, reagents were supplied for 4 – 30 min. Reagent supply was then switched off and the reactor tube was flushed with Ar. After cooling, the filter was recovered and weighed to determine how much material had collected on the upstream surface and inside the filter pores. For comparison across the three carbon sources, the collected masses were converted into a relative percentage by mass per unit area of filter cross-section per unit time.

2.3. Counter flow CH_4 experiments

Similar ratios of reagents were used as for the C^{13} experiments but the equipment was configured differently. Ferrocene, thiophene and the bulk H_2 flows were fed in as normal at the front of the quartz reactor tube, but CH_4 was only supplied in a counter flow

configuration, through a ¼" OD alumina tube whose position could be adjusted. The reactor was run in a "closed" manner, with an exit flange fitted with an exhaust line for the gases and a fitting to support the counter flow CH_4 line. Samples of CNT aerogel were collected for analysis by SEM (Leo Gemini 1530vp FEG-SEM).

3. Results and Discussion

3.1. Use of $C^{13}H_4$ to determine the contributions of different C species to CNT aerogel formation along the reactor axis

The Raman response of C^{13} has been used in various studies, for example to determine CNT growth mechanisms[31–33] and to identify the active carbon species in CNT carpet growth systems[34].

For our experiments, isotopically labeled methane ($C^{13}H_4$) was substituted for standard methane ($C^{12}H_4$) in the aerogel synthesis system to grow a CNT aerogel filament down the length of a quartz tube using the methodology described elsewhere[28] and in the Experimental Methods. On removal of the reactor tube after cooling in an Ar atmosphere, a fine filament had formed down the length of the reactor with bulk aerogel formation in the final section (see photograph and further explanation in S1).

The CNT filament was extracted from the reactor tube, split into sections and analysed by Raman spectroscopy. The characteristic Raman spectrum undergoes a downshift in wavenumber, where the degree of shift is proportional to the amount of C^{13} present in the sample, because of the modulation of phonon modes due to the heavier carbon nuclei[35]. Equation 1 shows this shift in wavenumber[33], where υ is the wavenumber of the C^{13} peak, υ_0 is the wavenumber of the equivalent C^{12} Raman peak, c_0 is the natural fraction of C^{13} in the environment (0.11%, therefore $c_0 = 0.011$) and c is the fraction of C^{13} in the sample. Using a typical C^{12} G-peak wavenumber of 1582 cm^{-1} measured using an ethanol-derived CNT aerogel on the same Raman with the same laser, a C^{13}-CNT sample would have a G-peak at 1521 cm^{-1}.

$$\upsilon = \upsilon_0 \sqrt{\frac{12+c_0}{12+c}} \qquad \text{Equation 1}$$

The Raman spectroscopy showed that the C^{13}:C^{12} ratio in the CNT aerogel material was essentially unchanged along the axis of the reactor, with samples generally being 94-99%

C^{13} (G peaks at ~1523 cm^{-1}) and only a sample at 50 mm upstream from the central point of the reactor tube showing a slightly lower C^{13} content (~92%). Within the precision of the technique (typical wavenumber resolution 4 cm^{-1}), these figures reflect the ratio of C^{13}:C^{12} input of 95.3:4.7 (see pie chart in Figure 2) therefore, carbon from CH_4 contributes to CNT formation equally at all points along the reactor profile, rather than being only dominant in the product after increased pyrolysis of CH_4 occurs. This also indicates that the carbon contribution from ferrocene and thiophene does not dominate in the CNTs synthesized in the areas where the decomposition of these species occur, as might be expected, and carbon available from decomposition products of thiophene and ferrocene play a subordinate role. The G:D ratio of the material, used as an indicator of CNT crystallinity, varies along the reactor axis, with the highest average G:D ratio of 9 occurring ~50 mm downstream of the location of the maximum temperature within the reactor. This axial change G:D ratio in the central reactor region reflects and maps with the overall changes in the product morphology previously observed[28] and is shown Figure 2 and Figure 3 where example C^{13} Raman spectra from different axial locations are shown alongside the corresponding product morphologies. While the highest G:D ratio does occur very close to the hottest point of the reactor profile, any possible effects of CNT annealing causing an increase in the G:D ratio due to the material residing in the hot zone for an extended time (i.e. during reactor cooling, prior to filament extraction) can be discounted, as the temperature did not exceed 1300 °C and the lowest temperatures typically inducing CNT annealing start at 1800 °C[4,36,37]. The lower G:D ratios of ~2.5 near the reactor inlet and ~3.5 at the reactor outlet indicate the presence of defects in the graphitized carbon species. Near the reactor entrance this is likely to be in the form of badly-graphitized carbon present in the catalytic nanoparticles seen decorating the CNT structures (Figure 3) but which have not produced CNTs, or may indicate a higher level of stone-wales defects in the CNT structures[38]. However, this is hard to determine from SEM images as CNT bundles are predominately formed in this process. At

the reactor exit, the formation of many badly-deformed CNTs is evident in the SEM. The G' peak, which is pronounced in the Figure 3 spectra, is an innate feature of sp^2 carbon structures, and relates to a longitudinal breathing-type mode of each individual hexagon in the lattice (figure 46 in [39]). While G' is an overtone of the D peak, it is an inelastic phonon emission process[40], independent of the elastic defect-related scattering processes which contribute to the D-peak[41,42]. Consequently, its intensity increases with decreasing defect concentration[42] i.e. in the presence of well-ordered sp^2 structures, in contrast to the D peak intensity. The ratio of G':D in our spectra follows the same trend as that of G:D, with a maximum ratio of ~7.5 coinciding with that of G:D = 9. The Raman observations show that not only the previously observed bulk product morphology[28] but also product crystallinity correlate with the spatial and temperature variations within a FC-CVD system.

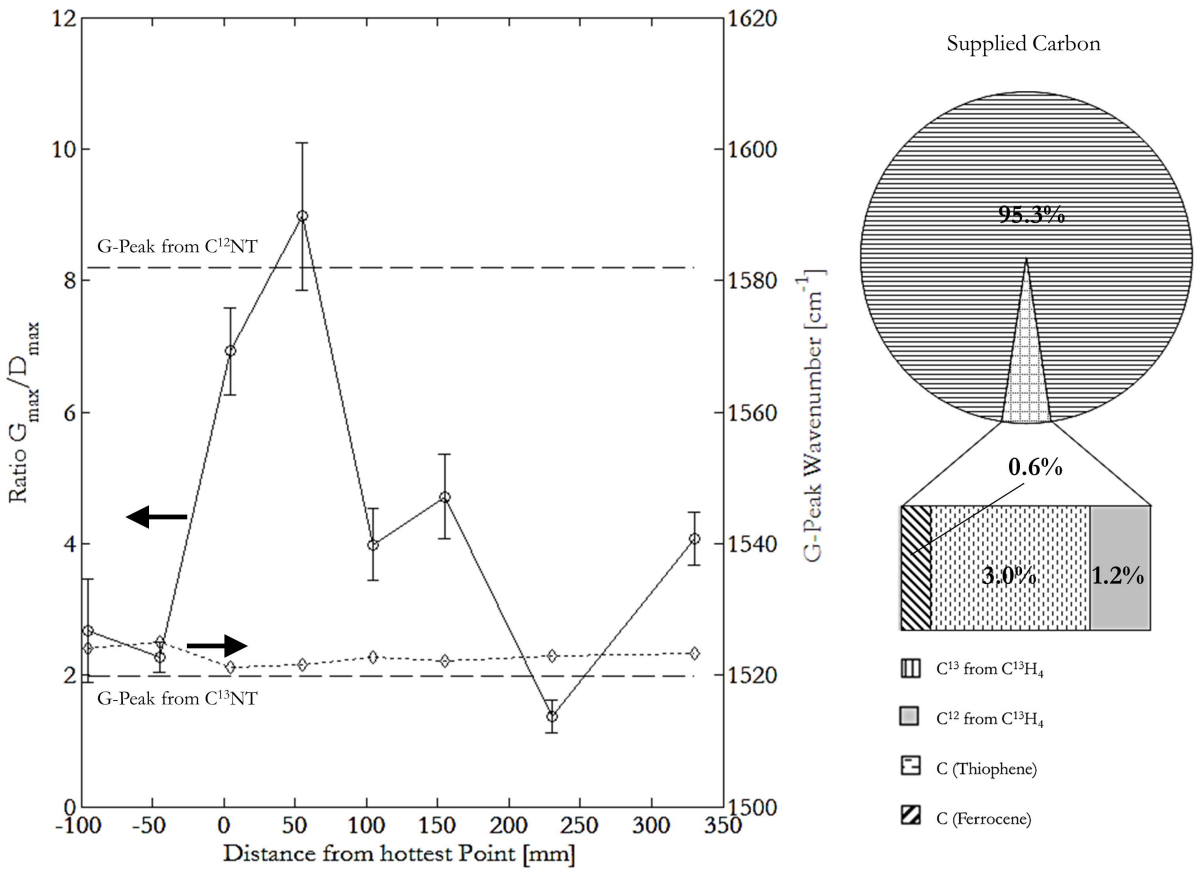

Figure 2. Graph showing the wavenumber of the G peak due to the presence of C^{13} in the aerogel sample as a function of axial position (open diamonds) and the G:D ratio of the CNT

aerogel in relation to the axial position of the material (open circles). Each data point is an average of four measurements and error bars indicate the standard error of the mean for a 90% confidence interval. The pie chart illustrates the total amount of C in the isotope-doped experiments that came from C^{13} compared to the remainder that came from thiophene, ferrocene and impurities in the C^{13} source.

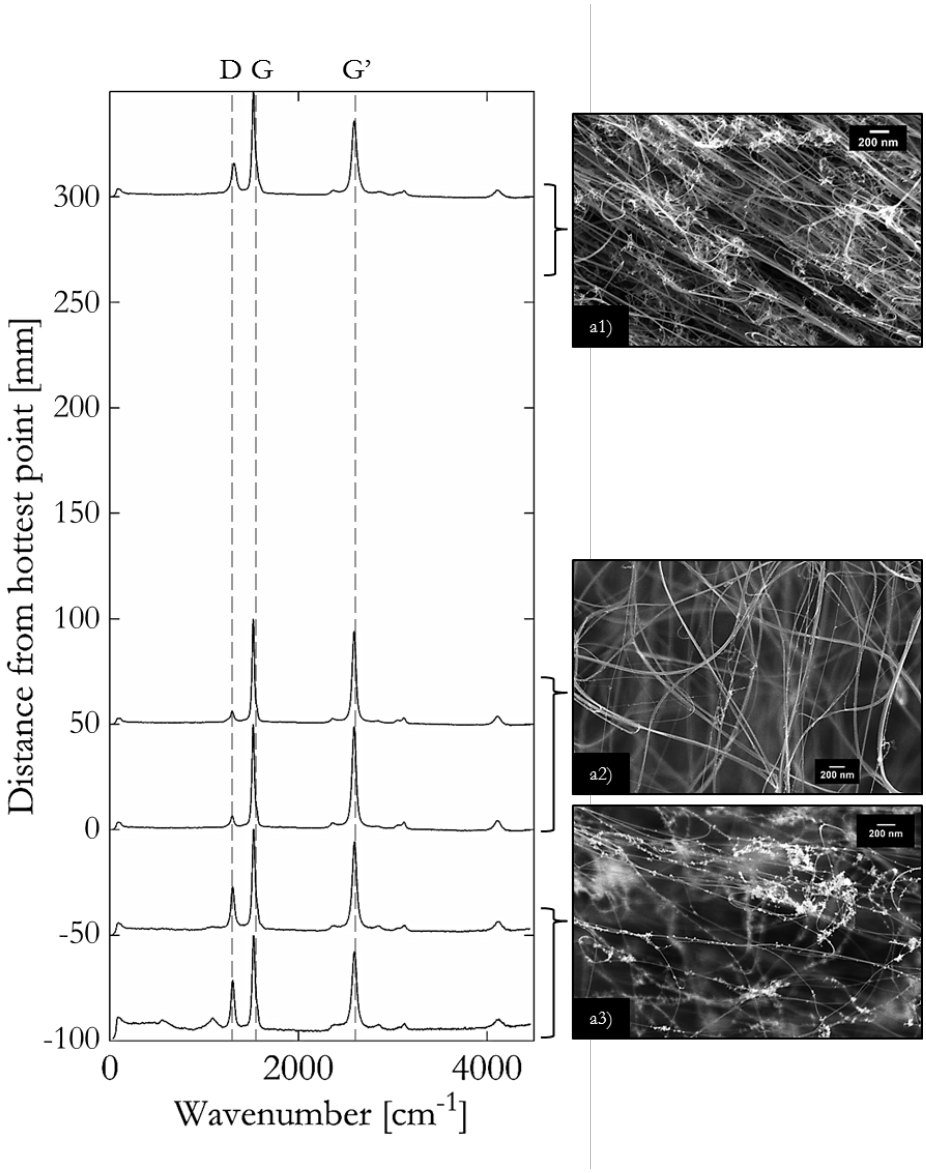

Figure 3. SEM study of different morphological features of the CNT aerogel compared with typical Raman spectra of C^{13} aerogel from the corresponding reactor location. The comparative heights of the G and D peak change along the axis, being highest at the centre of the reactor where the very clean CNT aerogel is seen in a2). Note that the wavenumbers of

the Raman features are all shifted from their regular C^{12} positions. The spectra are each normalized to the height of the G peak.

3.2. Quantification of aerogel formation along the reactor axis

A series of experiments were carried out to quantify axial aerogel production from different carbon sources, using the protocol described in the experimental section. A set of experiments were carried out using each carbon source, placing a filter firstly upstream of the hottest point in the reactor and subsequently in a series of positions between the hottest point and the reactor exit (illustrated in Figure 4). The mass of material collected at each location for each carbon source is shown in Figure 5. For all three carbon sources studied, the data points for the relative percentage by mass per unit area of filter cross-section per unit time along the reactor axis form a distinctive *S*-shaped curve. No significant difference in the bulk CNT formation was observed between the different carbon sources despite the fact that their decomposition temperatures vary.

With the filter in position b1) (x=-150 mm), the catalyst nanoparticles formed upstream of the filter mostly get filtered out (filtration efficiency >90%), leaving insufficient catalytic reagents to grow CNTs downstream, the presence of the filter at this location resulted in no downstream CNT aerogel formation. After use and exposure to air, the filter is covered with iron oxide and turned orange (photograph [A]). If the filter is positioned just upstream of the hottest point (b2, x=-50 mm) the aerogel forms as normal in the downstream section of the reactor. This shows that the majority of the catalytic nanoparticles have evaporated, passing through the filter in the vapor phase and re-nucleate downstream of the hottest point, facilitating the aerogel formation. Additionally, almost no CNT material was collected on filters placed just upstream of the hottest point of the axial temperature profile.

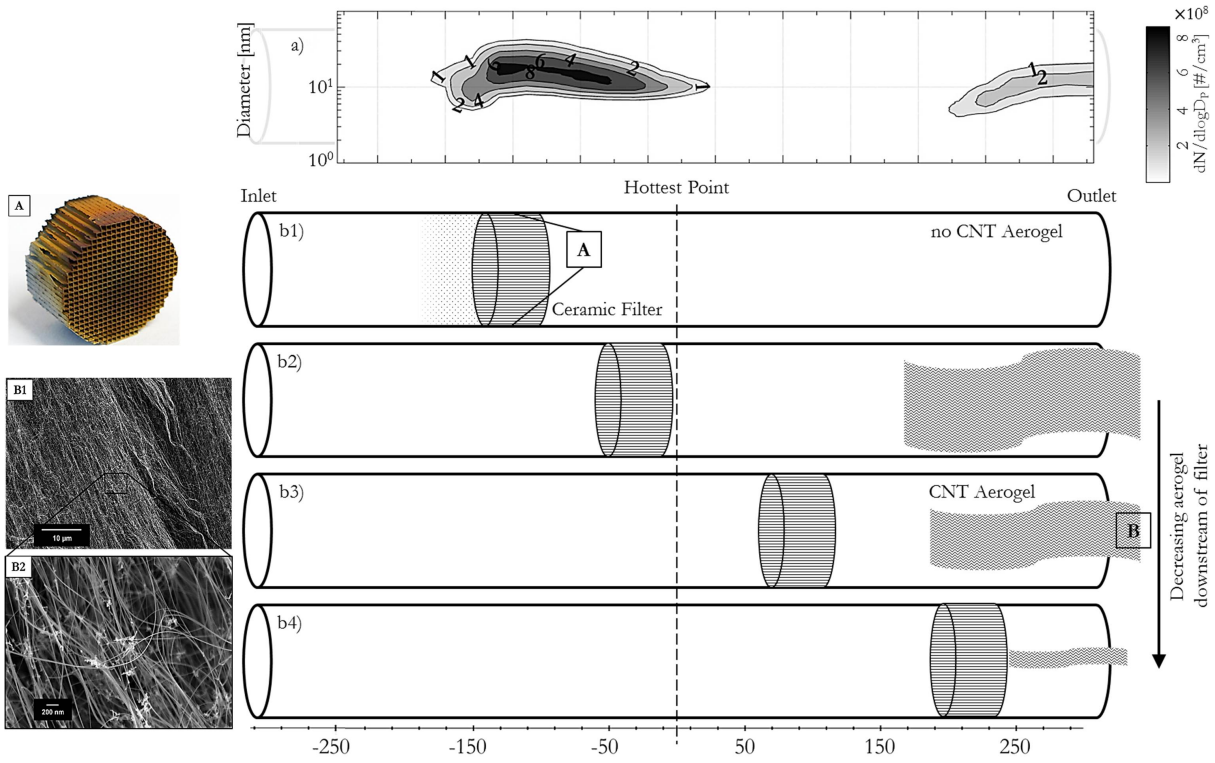

Figure 4. Graph a) is a representative measurement of the catalyst nanoparticle size distribution and concentration (shown as grayscale) along the reactor axis for furnace set points of ~1200 –1300°C, for a more detailed description see [28]. Schematic b1)-b4) shows the location of individual particle filters in separate experiments (at -150 mm, -50 mm, 70 mm and 200mm relative to the hottest point of the reactor temperature profile respectively) and their impact on aerogel formation. The inset photograph A shows a particle filter which was positioned in the middle of the nucleation zone and traps the majority of the nanoparticles, preventing aerogel formation downstream. Photographs B1 and B2 show representative SEM images of CNT web collected at the outlet of the reactor.

Downstream of the maximum temperature, the vast majority of aerogel production occurred as the temperature started to drop, with the largest amount of the material being synthesized as the reactor temperature passed from ~1200 °C to ~950 °C (Figure 4 filter positions b3, x=70 mm and b4, x=200 mm). This region corresponds

to the location of catalyst particle re-nucleation in the reactor as shown in Figure 4.a, which shows how catalyst particles form, evaporate and re-nucleate as they pass down the reactor[28]. The correlation between this data and the qualitative observations previously made regarding the location of the majority of the aerogel growth indicates that the majority of CNT growth within the reactor coincides with, and is caused by, the re-nucleation of catalyst particles after the flow has cooled from the hottest part of the reactor. Some aerogel formation still occurs downstream of the filters in positions b3 and b4 but in smaller amounts as an increasing proportion of the aerogel formation is happening upstream and is then trapped. The CNTs formed upstream of the filter lead to the build-up of a filter cake and eventual clogging over time. However, this built-up material on the upstream filter surface ensures that virtually all solid masses upstream of the alumina filter were collected, aiding the accuracy of the data presented in Figure 5. Also, even after filter cake build-up and ensuring complete filtration, CNT aerogel formation was observed downstream of the filter as described in Figure 4. One of the consequences of the downstream bulk-aerogel formation is that the nature of the carbon species contributing to the growth needs further consideration. If the material was principally forming in the first portion of the reactor, before the carbon sources pass through the most elevated part of the temperature profile, then the CNTs in the aerogel could be assumed to be growing from the direct catalytic decomposition of the supplied carbon source only. However, formation of the aerogel after the hottest part of the temperature profile means that pyrolysis will have occurred to some degree and the range of carbon species present to react with the re-nucleating catalytic nanoparticles, which are at this point very small liquid catalyst nanoparticle droplets[26], will be much more diverse[43].

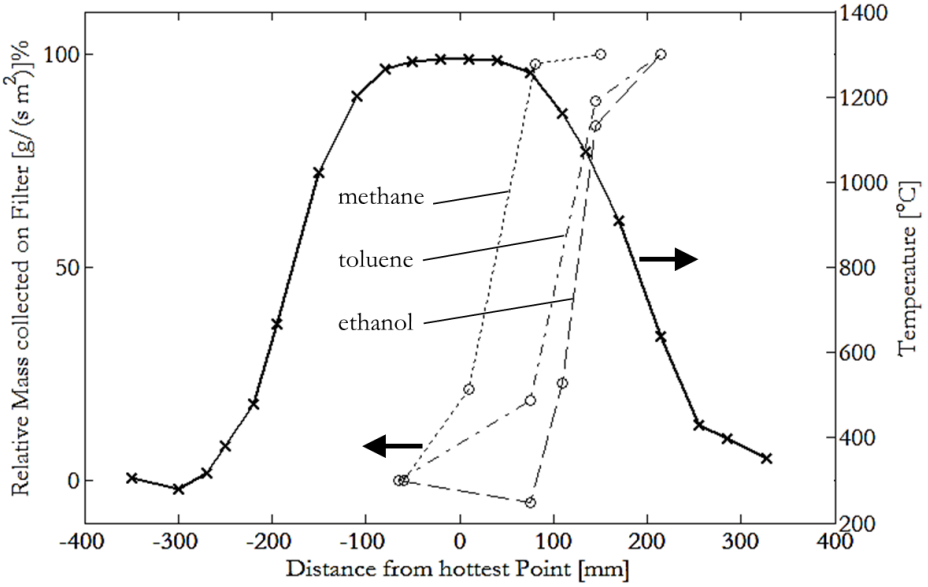

Figure 5. Mass of CNT aerogel material collected at different locations along the reactor axis on alumina filters when using CH_4, toluene and ethanol respectively as the CNT hydrocarbon source. The mass plots are overlaid with the reactor temperature profile.

The presence of increasing concentrations of alkyne-like pyrolytic species with temperature when ferrocene, thiophene or CH_4 were decomposed in a H_2 environment were observed by FTIR[28], providing evidence to support the idea that pyrolytic species play a major role in the bulk aerogel formation. To determine the influence of pyrolytic carbon species with re-nucleating catalytic nanoparticles on the bulk aerogel formation, the carbon source was supplied only to the cooling zone of the reactor, in a counter flow manner as shown in Figure 6. The counter-flow CH_4 (20 – 70 sccm) was determined to have a depth of the penetration of up to ~40 mm beyond the tube tip depending on the injection flowrate (see supplementary information S3). By changing the position of the alumina tube, CH_4 could either be supplied upstream of the catalytic nanoparticle re-nucleation zone, allowing the jet of CH_4 to reach the hottest part of the reactor temperature profile before subsequently passing back through the catalytic nanoparticle re-nucleation zone in which presumably the smallest catalyst nanoparticle droplets are present, just downstream from the hottest point in the reactor (see Figure

4.a). Alternatively, the CH_4 could be supplied so that the catalytic re-nucleation zone received only CH_4, unaffected by the elevated temperatures of the hottest zone. When CH_4 was injected so that the jet was supplied only to the catalytic nanoparticle re-nucleation zone at a temperature profile position of ~900 °C, no aerogel was formed, indicating that CH_4 was not interacting with the catalytic nanoparticles to produce CNTs. An aerogel only started to form when the CH_4 supply tube was inserted further, therefore allowing the CH_4 jet to reach the hottest part of the reactor (the 'Critical Injection Point' indicated in Figure 6). The CNT aerogel formed in a typical manner as depicted in the previous electron microscope images (see Figure 4). However, samples collected under these conditions contained many graphitic impurities as shown in the SEM images in Figure 6 but the system was not optimized for CNT purity. These results highlight the key role that pyrolytic carbon species are playing in this system. In fact, it is likely that the interaction of small catalyst nanoparticle droplets (detected average $d_p \approx 10$ nm), just downstream of the hottest point in the reactor, which have the ideal size and composition, with the carbon source and its pyrolytic compounds is essential to the bulk aerogel formation process. Future enhancements in CNT production and purity are likely to arise from optimization of the downstream processes, co-locating delivery of pyrolytic compounds and catalyst particles.

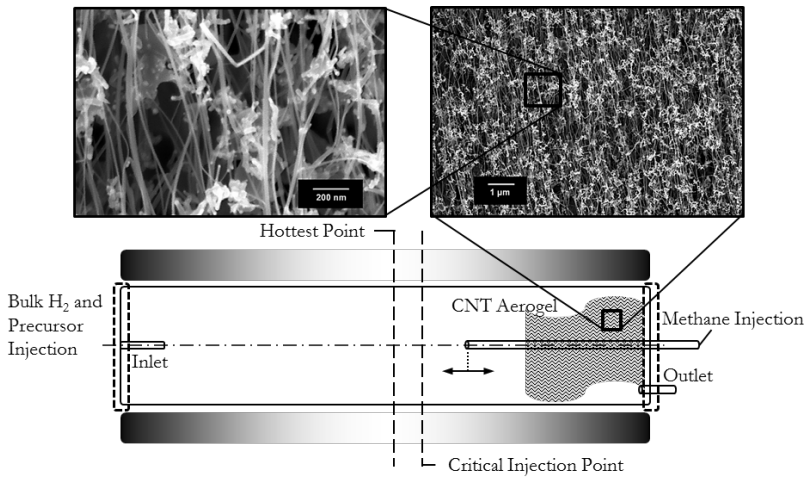

Figure 6. Schematic of reactor configuration to supply the hydrocarbon source to various locations on the downstream temperature profile of the CVD reactor. The supply tube position is adjustable, such that CH_4 could be supplied either upstream of, or directly to the re-nucleation zone. SEM images of the aerogel material formed when CH_4 was supplied upstream of the nucleation zone are inset.

4. Conclusion

In summary, we have shown that the pyrolytic compounds from the carbon precursor decomposition are key to the bulk CNT aerogel formation in the FC-CVD reactor. The source of carbon within the CNTs was tracked by isotopically-labelled methane ($C^{13}H_4$) and analysed with Raman spectroscopy. The results show the origin of the carbon in the CNT aerogel to be equal to the ratio in which it is supplied with ~95% coming from the carbon source (methane) throughout the entire reactor with carbon from the iron and sulphur precursors (ferrocene and thiophene) not dominating in the early parts of the reactor. The initial catalytic nanoparticle nucleation zone only yields small quantities of CNT aerogel via catalytic cracking of CH_4, compared to the catalytic nanoparticle re-nucleation zone where the bulk aerogel forms. It was also possible to link both the product morphologies of the CNT aerogel and the crystallinity of the formed material to the temperature profile and nanoparticle size distributions along the reactor axis.

The axial production rate of CNTs within a CVD reactor was measured for the first time using alumina filters to collect all solid mass from the gas flow. The axial rates of production showed that the bulk formation of CNTs primarily occurs in the downstream portion of the reactor after the maximum temperature. These results indicate that CNT formation is primarily linked to catalyst re-nucleation as the evaporated catalyst species (Fe and S) condense to form catalysts droplets of a size capable of CNT formation (d_p≈10 nm, compare Figure 4.a). Furthermore, determining the mass of the CNT aerogel formation facilitated a study of the effect of different carbon precursors on the bulk aerogel formation. Within experimental uncertainties, the bulk CNT aerogel formation happens at very similar locations in the FC-CVD reactor, downstream of the hottest point, independent of the nature of the carbon source.

Investigation into the contribution of pyrolytic carbon species derived from CH_4 were investigated by changing the axial location of CH_4 injection into the reactor, and thus the time-temperature profile it encountered. We found that CH_4 must be exposed to temperatures greater than 1000 °C to stimulate CNT aerogel formation when injected independently from the catalyst precursors. As the pyrolytic formation of hydrocarbon radicals is linked to the incurred temperature, these results indicate that not only are suitable catalyst nanoparticles needed for bulk CNT aerogel formation, but also the provision of activated carbon species to the catalysts. The interaction of small catalyst nanoparticle droplets just downstream of the hottest point in the reactor, with the carbon source and its pyrolytic compounds is then crucial for bulk CNT aerogel formation.

While these results change the view of CNT formation within FC-CVD reactors, further study is needed on the radial distribution of precursors, radicals, catalysts and CNTs within the chamber. Emerging techniques, such as laser light scattering, in-situ Raman, and laser induced incandescence are necessary next steps for full reactor characterization. As CNT production increases to large-scale reactors, a more detailed understanding of the formation processes will be necessary before full control of the reaction volume can be achieved allowing CNT production at industrially-desired quantities.

Acknowledgements

The authors thank Q-Flo Ltd for providing funding towards this research; C. Hoecker additionally thanks Churchill College Cambridge for financial support. C. Hoecker and F. Smail contributed equally to this work.

[1] Nanocomp Technologies Inc, http://www.nanocomptech.com/quick-links, (accessed June 2016), (n.d.). http://www.nanocomptech.com/quick-links (accessed June 5, 2016).

[2] Tortech Nano Fibers Ltd, (n.d.). http://tortechnano.com/tortech-nano-fibers (accessed June 5, 2016).

[3] teijinaramid, http://www.teijinaramid.com/2013/01/twaron-spinning-process-is-key-to-carbon-nanotube-fiber-breakthrough/, (accessed June 2016), (n.d.). http://www.teijinaramid.com/2013/01/twaron-spinning-process-is-key-to-carbon-nanotube-fiber-breakthrough/ (accessed June 5, 2016).

[4] J.F. Niven, M.B. Johnson, S.M. Juckes, M.A. White, N.T. Alvarez, V. Shanov, Influence of annealing on thermal and electrical properties of carbon nanotube yarns, Carbon N. Y. 99 (2016) 485–490. doi:10.1016/j.carbon.2015.12.014.

[5] H.J. Kim, J. Lee, B. Park, J.-H. Sa, A. Jung, T. Kim, J. Park, W. Hwang, K.-H. Lee, Improving the tensile strength of carbon nanotube yarn via one-step double [2+1] cycloadditions, Korean J. Chem. Eng. 33 (2016) 299–304. doi:10.1007/s11814-015-0140-9.

[6] N.T. Alvarez, P. Miller, M. Haase, N. Kienzle, L. Zhang, M.J. Schulz, V. Shanov, Carbon nanotube assembly at near-industrial natural-fiber spinning rates, Carbon N. Y. 86 (2015) 350–357. doi:10.1016/j.carbon.2015.01.058.

[7] Y.-L. Li, I. a Kinloch, A.H. Windle, Direct spinning of carbon nanotube fibers from chemical vapor deposition synthesis., Science. 304 (2004) 276–8. doi:10.1126/science.1094982.

[8] H. Xu, X. Tong, Y. Zhang, Q. Li, W. Lu, Mechanical and electrical properties of laminated composites containing continuous carbon nanotube fi lm interleaves, Compos. Sci. Technol. 127 (2016) 113–118. doi:10.1016/j.compscitech.2016.02.032.

[9] W. Xu, Y. Chen, H. Zhan, J.N. Wang, High-Strength Carbon Nanotube Film from

Improving Alignment and Densification, Nano Lett. (2016) acs.nanolett.5b03863. doi:10.1021/acs.nanolett.5b03863.

[10] T. Wu, J.N. Wang, Carbon nanotube springs with high tensile strength and energy density, RSC Adv. 6 (2016) 38187–38191. doi:10.1039/C6RA05464A.

[11] A. Mikhalchan, Z. Fan, T.Q. Tran, P. Liu, V.B.C. Tan, T.-E. Tay, H.M. Duong, Continuous and scalable fabrication and multifunctional properties of carbon nanotube aerogels from the floating catalyst method, Carbon N. Y. 102 (2016) 409–418. doi:10.1016/j.carbon.2016.02.057.

[12] M.F.L. De Volder, S.H. Tawfick, R.H. Baughman, A.J. Hart, Carbon Nanotubes: present and Future Commercial applications, Science (80-.). 339 (2013) 535–539. doi:10.1126/science.1222453.

[13] Q. Zhang, J.Q. Huang, W.Z. Qian, Y.Y. Zhang, F. Wei, The road for nanomaterials industry: A review of carbon nanotube production, post-treatment, and bulk applications for composites and energy storage, Small. 9 (2013) 1237–1265. doi:10.1002/smll.201203252.

[14] A. Lekawa-Raus, J. Patmore, L. Kurzepa, J. Bulmer, K. Koziol, Electrical Properties of Carbon Nanotube Based Fibers and Their Future Use in Electrical Wiring, Adv. Funct. Mater. 24 (2014) 3661–3682. doi:10.1002/adfm.201303716.

[15] D. Janas, K.K. Koziol, A review of production methods of carbon nanotube and graphene thin films for electrothermal applications., Nanoscale. 6 (2014) 3037–45. doi:10.1039/c3nr05636h.

[16] M.S. Motta, A. Moisala, I.A. Kinloch, A.H. Windle, The role of sulphur in the synthesis of carbon nanotubes by chemical vapour deposition at high temperatures., J. Nanosci. Nanotechnol. 8 (2008) 2442–2449. doi:10.1166/jnn.2008.500.

[17] G.G. Tibbetts, C.A. Bernardo, D.W. Gorkiewicz, R.L. Alig, Role of sulfur in the production of carbon fibers in the vapor phase, Carbon N. Y. 32 (1994) 569–576.

doi:10.1016/0008-6223(94)90074-4.

[18] R.M. Sundaram, A.H. Windle, Effect of Carbon Precursors on the Structure and Properties of Continuously Spun Carbon Nanotube Fibers, Sci. Adv. Mater. 7 (2015) 643–653. doi:10.1166/sam.2015.2147.

[19] J. Wei, H. Zhu, Y. Jia, Q. Shu, C. Li, K. Wang, B. Wei, Y. Zhu, Z. Wang, J. Luo, W. Liu, D. Wu, The effect of sulfur on the number of layers in a carbon nanotube, Carbon N. Y. 45 (2007) 2152–2158. doi:10.1016/j.carbon.2007.07.001.

[20] R. Rao, N. Pierce, X. Zhang, R. Wheeler, B. Maruyama, S. Talapatra, Understanding the Role of Sulfur in Tuning the Diameter and Morphology in the Chemical Vapor Deposition Growth of Carbon Nanotubes, Mater. Express. 1 (2011) 160–166. doi:10.1166/mex.2011.1019.

[21] V. Reguero, B. Alemán, B. Mas, J.J. Vilatela, Controlling Carbon Nanotube Type in Macroscopic Fibers Synthesized by the Direct Spinning Process, Chem. Mater. 26 (2014) 3550–3557.

[22] W. Ren, W. Ren, F. Li, F. Li, S. Bai, S. Bai, H.M. Cheng, H.M. Cheng, The effect of sulfur on the structure of carbon nanotubes produced by a floating catalyst method, 6 (2006) 1339–1345. doi:10.1166/jnn.2006.301.

[23] R.M. Sundaram, K.K.K. Koziol, A.H. Windle, Continuous direct spinning of fibers of single-walled carbon nanotubes with metallic chirality., Adv. Mater. 23 (2011) 5064–8. doi:10.1002/adma.201102754.

[24] T. Gspann, F. Smail, A. Windle, Spinning of carbon nanotube fibres using the floating catalyst high temperature route: purity issues and the critical role of sulphur, Faraday Discuss. 173 (2014) 2–7. doi:10.1039/C4FD00066H.

[25] C. Paukner, K.K.K. Koziol, Ultra-pure single wall carbon nanotube fibres continuously spun without promoter., Sci. Rep. 4 (2014) 3903. doi:10.1038/srep03903.

[26] A. Moisala, A.G. Nasibulin, E.I. Kauppinen, The role of metal nanoparticles in the

catalytic production of single-walled carbon nanotubes—a review, J. Phys. Condens. Matter. 15 (2003) S3011–S3035. doi:10.1088/0953-8984/15/42/003.

[27] M. Picher, E. Anglaret, R. Arenal, V. Jourdain, Processes controlling the diameter distribution of single-walled carbon nanotubes during catalytic chemical vapor deposition, ACS Nano. 5 (2011) 2118–2125. doi:10.1021/nn1033086.

[28] C. Hoecker, F. Smail, M. Bajada, M. Pick, A. Boies, Catalyst nanoparticle growth dynamics and their influence on product morphology in a CVD process for continuous carbon nanotube synthesis, Carbon N. Y. 96 (2016) 116–124. doi:10.1016/j.carbon.2015.09.050.

[29] I. Kunadian, R. Andrews, D. Qian, M. Pinar Mengüç, Growth kinetics of MWCNTs synthesized by a continuous-feed CVD method, Carbon N. Y. 47 (2009) 384–395. doi:10.1016/j.carbon.2008.10.022.

[30] M. Kumar, Y. Ando, Chemical vapor deposition of carbon nanotubes: a review on growth mechanism and mass production., J. Nanosci. Nanotechnol. 10 (2010) 3739–3758. doi:10.1166/jnn.2010.2939.

[31] M. Pinault, V. Pichot, H. Khodja, P. Launois, C. Reynaud, M. Mayne-L'Hermite, Evidence of sequential lift in growth of aligned multiwalled carbon nanotube multilayers, Nano Lett. 5 (2005) 2394–2398. doi:10.1021/nl051472k.

[32] R. Xiang, Z. Zhang, K. Ogura, J. Okawa, E. Einarsson, Y. Miyauchi, J. Shiomi, S. Maruyama, Vertically Aligned 13 C Single-Walled Carbon Nanotubes Synthesized by No-Flow Alcohol Chemical Vapor Deposition and their Root Growth Mechanism, Jpn. J. Appl. Phys. 47 (2008) 1971–1974. doi:10.1143/JJAP.47.1971.

[33] H. Ago, N. Ishigami, N. Yoshihara, K. Imamoto, S. Akita, Visualization of Horizontally-Aligned Single-Walled Carbon Nanotube Growth with Isotopes, J. Phys. Chem. C. 112 (2008) 1735–1738.

[34] Y.-Q. Xu, E. Flor, H. Schmidt, R.E. Smalley, R.H. Hauge, Effects of atomic hydrogen

and active carbon species in 1 mm vertically aligned single-walled carbon nanotube growth, Appl. Phys. Lett. 89 (2006) 123116. doi:10.1063/1.2349280.

[35] Y. Miyauchi, S. Maruyama, Identification of an excitonic phonon sideband by photoluminescence spectroscopy of single-walled carbon-13 nanotubes, Phys. Rev. B. 74 (2006) 35415. doi:10.1103/PhysRevB.74.035415.

[36] K. Behler, S. Osswald, H. Ye, S. Dimovski, Y. Gogotsi, Effect of Thermal Treatment on the Structure of Multi-walled Carbon Nanotubes, J. Nanoparticle Res. 8 (2006) 615–625. doi:10.1007/s11051-006-9113-6.

[37] Y.A. Kim, H. Muramatsu, T. Hayashi, M. Endo, M. Terrones, M.S. Dresselhaus, Thermal stability and structural changes of double-walled carbon nanotubes by heat treatment, Chem. Phys. Lett. 398 (2004) 87–92. doi:10.1016/j.cplett.2004.09.024.

[38] P.T. Araujo, M. Terrones, M.S. Dresselhaus, Defects and impurities in graphene-like materials, Mater. Today. 15 (2012) 98–109. doi:10.1016/S1369-7021(12)70045-7.

[39] M.S. Dresselhaus, P.C. Eklund, Phonons in carbon nanotubes, Adv. Phys. 49 (2000) 705–814. doi:10.1080/000187300413184.

[40] M.S. Dresselhaus, G. Dresselhaus, A. Jorio, A.G. Souza Filho, R. Saito, Raman spectroscopy on isolated single wall carbon nanotubes, Carbon N. Y. 40 (2002) 2043–2061. doi:10.1016/S0008-6223(02)00066-0.

[41] a. Souza Filho, a. Jorio, G. Dresselhaus, M. Dresselhaus, R. Saito, a. Swan, M. Ünlü, B. Goldberg, J. Hafner, C. Lieber, M. Pimenta, Effect of quantized electronic states on the dispersive Raman features in individual single-wall carbon nanotubes, Phys. Rev. B. 65 (2001) 1–6. doi:10.1103/PhysRevB.65.035404.

[42] J. Maultzsch, S. Reich, C. Thomsen, S. Webster, R. Czerw, D.L. Carroll, S.M.C. Vieira, P.R. Birkett, C.A. Rego, Raman characterization of boron-doped multiwalled carbon nanotubes, Appl. Phys. Lett. 81 (2002) 2647–2649. doi:10.1063/1.1512330.

[43] O. Olsvik, O. a Rokstad, a Holmen, Pyrolysis of Methane in the Presence of Hydrogen,

Chem. Eng. Technol. 18 (1995) 349–358. doi:DOI 10.1002/ceat.270180510.